Applied Catalysis B: Environment and Energy 381 (2026) 125902

Contents lists available at ScienceDirect

Applied Catalysis B: Environment and Energy

journal homepage: www.elsevier.com/locate/apcatb

Which dominates CO_2 to CO electroreduction from low to industrial current density: Catalyst activity or CO_2 availability?

Guoliang Chen [a], Min Hong [a,b], Beibei Ma [c], Yizhu Kuang [a], Hesamoddin Rabiee [d], Xiaomin Xu [e], Fatereh Dorosti [a,c], Penghui Yan [c], Nilam Shah [c], Ashok Kumar Nanjundan [a,b], Zhonghua Zhu [c], Hao Wang [a,b,*], Lei Ge [a,b,*]

[a] Centre for Future Materials, University of Southern Queensland, Springfield, QLD 4300, Australia
[b] School of Engineering, University of Southern Queensland, Springfield, QLD 4300, Australia
[c] School of Chemical Engineering, The University of Queensland, Brisbane, QLD 4072, Australia
[d] University of Bern, Department of Chemistry, Biochemistry and Pharmaceutical Sciences, Freiestrasse 3, Bern 3012, Switzerland
[e] Curtin Centre for Advanced Energy Materials and Technologies (CAEMT), WA School of Mines: Minerals, Energy and Chemical Engineering (WASM-MECE), Curtin University, Perth, Western Australia 6102, Australia

ARTICLE INFO

Keywords:
Gas diffusion electrodes
CO_2 to CO electroreduction
Hollow fibre
Flow-through
CO_2 availability

ABSTRACT

Electrochemical reduction of CO_2 (CO_2RR) offers a sustainable route for converting renewable electricity into value-added chemicals. However, scaling CO_2RR to industrially relevant current densities remains challenging due to intrinsic kinetics barriers, competing side reactions such as the hydrogen evolution reaction (HER), and limitations in CO_2 mass transport. To elucidate whether catalyst activity or CO_2 availability dominates CO_2RR performance across current densities, we engineered flow-through hollow fiber gas diffusion electrodes (HFGDEs) integrated with in-situ grown, defect-rich silver nanosheets. At low current densities, catalytic activity is the primary determinant. The developed HFGDE with defect-rich silver nanosheets yields a high Faradaic efficiency of CO of 93.5 % at −0.8 (V vs. RHE), attributed to enhanced adsorption of *COOH intermediate on silver defect sites, as confirmed by in-situ Raman spectroscopy and density functional theory (DFT) calculations. However, as the system scales to industrially relevant current densities (up to 500 mA/cm^2), CO_2 availability becomes the dominant limitation due to the intensified fight between CO_2 and H_2O for electrons. The HFGDE architecture addresses this challenge by continuously supplying convective CO_2 flow to the active sites, enabling a CO partial current density of 381.8 mA/cm^2 under a total current density of 500 mA/cm^2. These findings highlight that while catalyst activity governs CO_2RR performance at lower current densities, adequate CO_2 supply is essential to maintain high selectivity and suppress HER under industrial conditions.

1. Introduction

The excessive consumption of fossil fuels has led to a sharp rise in atmospheric CO_2 levels, intensifying the greenhouse effect and exacerbating climate change [1]. Therefore, it is urgent to develop effective CO_2 capture, storage, and conversion techniques to mitigate atmospheric CO_2 concentrations [2,3]. Among various techniques, the electrochemical reduction reaction of CO_2 (CO_2RR) driven by renewable electricity stands out as a promising solution for converting CO_2 into valuable chemicals, such as carbon monoxide (CO), formic acid, and alcohol [4–10]. CO, in particular, holds significant industrial value, serving as a key feedstock in processes like Fischer-Tropsch synthesis [11].

Despite significant progress, achieving high selectivity and activity for CO production remains challenging, largely due to the competitive hydrogen evolution reaction (HER) and the high activation barrier associated with CO_2 activation [12,13]. To overcome these limitations, considerable effort has been devoted to developing electrocatalysts with high intrinsic activity, strong CO_2 binding capabilities, and enhanced reaction kinetics. Strategies such as morphology control, alloying, and nanostructure reconstruction have been widely employed to improve catalytic performance [14–18]. Among these, defect engineering has emerged as a particularly effective approach [19,20]. The introduction of structural defects can modify the electronic and geometric properties

* Corresponding authors at: Centre for Future Materials, University of Southern Queensland, Springfield, QLD 4300, Australia.
E-mail addresses: hao.wang@usq.edu.au (H. Wang), lei.ge@usq.edu.au (L. Ge).

https://doi.org/10.1016/j.apcatb.2025.125902
Received 19 May 2025; Received in revised form 3 August 2025; Accepted 29 August 2025
Available online 30 August 2025

of the catalyst surface, generating unsaturated coordination sites that enhance the adsorption and stabilization of key CO_2RR intermediates, thereby improving selectivity and activity. For instance, defect-rich silver nanocrystals have demonstrated near 100 % Faradaic efficiency for CO production at low current densities [21], while lattice-dislocated bismuth nanowires have shown high Faradaic efficiency for formate production [22].

However, as CO_2RR systems are scaled to industrially relevant current densities, particularly in the range of hundreds of mA/cm^2 to ampere-level, CO_2 availability becomes a critical factor [23,24]. At these high current densities, the rapid consumption of CO_2 at the catalytic sites intensifies competition between CO_2 and water for electrons. When CO_2 is insufficiently supplied to the active sites, the HER becomes the dominant reaction, severely reducing CO selectivity and overall efficiency. Therefore, electrocatalysts must be integrated with gas-diffusion electrodes within flow cell configurations to evaluate their CO_2RR performance at high current densities. Conventional GDEs, however, are typically composed of multiple layers, including a gas diffusion layer, microporous layer, and catalyst layer, where the catalyst is mixed with polymeric binders such as Nafion ionomer and PTFE, then coated onto a carbon substrate [6,25]. While widely used, this multilayer structure introduces complexity, reduces mechanical robustness, and often leads to variability in catalyst utilization and stability, making it difficult to isolate the intrinsic catalytic behavior. In contrast, self-supported hollow fiber gas diffusion electrodes (HFGDEs) can simplify cell structure by utilizing the lumen side as a gas chamber [26–29]. The CO_2 gas is directly fed into the lumen side of the hollow fiber, where it penetrates through the hollow fiber walls to reach active sites, ensuring sufficient CO_2 delivery at the triple-phase interfaces. In addition, HFGDEs can serve as conductive and mechanically robust substrates for the in situ growth of electrocatalysts. This strategy eliminates the need for polymeric binders and enhances catalyst exposure, electron transport, and mass transfer. More importantly, it also avoids complications associated with immobilization, such as reduced activity or stability, which are often observed with powder-based electrocatalysts coated on conventional GDEs [30]. This renders the HFGDE a suitable platform for probing CO_2RR performance across a wide current density range from low to industrially relevant current densities.

Herein, we design and fabricate a flow-through hollow fiber gas-diffusion electrode with in-situ grown, defect-rich silver nanosheets (D-AgNS HF) to systematically investigate the dominant factor, catalyst activity or CO_2 availability, that governs CO_2 to CO electroreduction across current densities up to 500 mA/cm^2. Our method leverages the unique structure of HFGDEs to bridge the performance evaluation gap in a simple H-Cell setup within a consistent electrode configuration. The same HFGDE can be operated in both non-GDE and GDE modes by simply altering the way of CO_2 feed, either through dissolution in the bulk electrolyte (non-GDE condition) or via direct gas flow through the lumen of the hollow fiber (GDE condition). Our findings reveal that at low current densities, both Ag HF and D-AgNS HF electrodes achieve high CO selectivity even with limited CO_2 supply (non-GDE condition), indicating that CO_2 availability is not the limiting factor under these conditions. However, as the current density increases from 50 to 500 mA/cm^2, a sharp decrease in CO selectivity is observed. This highlights that at industrial-level current densities, the competition between water and CO_2 for electrons intensifies, making CO_2 availability the dominant factor in determining reaction outcomes. The hollow fiber operated in GDE mode delivers significantly higher partial current densities for CO production compared to the same electrode operated in non-GDE mode, which confirms that the flow-through HFGDE configuration not only improves CO_2 mass transport but also promotes more efficient triple-phase boundary formation, thereby accelerating CO_2RR kinetics.

2. Experimental method

Chemicals and materials, and the fabrication of Cu hollow fiber, are provided in the Supporting Information.

2.1. Fabrication of defect-rich silver nanosheet-based HFGDE (D-AgNS HF)

The preparation of silver hollow fiber (Ag HF) was done using a galvanic replacement process. A 0.1 M silver ammonium solution was prepared by dropping NH_4OH into 0.1 M $AgNO_3$ solution under vigorous magnetic stirring. Then, those fresh Cu HFGDEs were immersed in 0.1 M silver ammonium solution under orbital shaking at 160 rpm for 2 h. The transparent solution turned to dark blue with copper color from Cu HF, turning to white silver color. The as-prepared samples were washed with DI water several times, flushed with nitrogen, and stored in a nitrogen atmosphere.

The defect-rich silver nanosheet-based hollow fiber (D-AgNS HF) was prepared by electrooxidation and reduction of Ag HF. The electrooxidation of Ag HF was performed in a three-electrode system, with a Pt mesh as a counter electrode and an Ag/AgCl with 3 M NaCl solution working as a reference electrode. The Ag HF as a working electrode was immersed in 0.2 M NaOH, applying a single linear scanning voltammetry (LSV) with a scanning rate of 5 mV/s from a potential range of −0.2 to −0.8 (V vs. RHE). The white of Ag HF turned black. The as-prepared samples were washed with DI water and flushed with nitrogen. The reduction of oxidized Ag HF was performed in a CO_2-saturated 0.5 M $KHCO_3$ under −5 mA/cm^2 for 600 s. The black oxidized Ag HF turned to a dark grey color. The as-prepared D-AgNS HF was washed with DI water and stored in a nitrogen atmosphere after being flushed with nitrogen.

2.2. Characterizations

The surface and cross-section morphology of HFGDEs were observed by scanning electron microscopy (SEM, JOEL-7100 F) coupled with an energy-dispersive X-ray analyser (EDX) for elemental mapping. The morphology and thickness of silver nanosheets were investigated on an atomic force microscope (Bruker MultiMode 8) at a Scanasyst-Air mode. The cantilever of the probe (Scanasyst-Air) used in all specimens has a spring constant of 0.4 N/m and a tip radius of 2 μm. The nanostructures of defect-rich silver nanosheets were inspected by a Field Emission Transmission Electron Microscope (FETEM, Hitachi HF 5000, Japan). The crystalline structures of the bulk phase HFGDEs were analyzed by X-ray diffraction (XRD, Bruker advanced X-ray diffractometer, Cu Kα (λ=1.5405Å) radiation source, Japan). X-ray photoelectron spectroscopy (XPS) was applied to analyze the surface valence state and surface compositions of the HFGDEs. XPS was conducted on a Kratos Axis ULTRA XPS with a monochromatic Al Kα radiation source (1486.6 eV) at 15 kV (10 mA) and a hemispherical electron energy analyzer (165 nm). CASA® software was used to analyze the XPS data, calibrated to the C 1 s signal at 284.4 eV as the reference. NEXAFS experiments were performed at the Soft X-ray Spectroscopy (SXR) beamline at the Australian Synchrotron, ANSTO. Spectra were collected in the total electron yield mode at a 55° incident angle. Data were analyzed using the QANT software package. To examine the adsorption and desorption characteristics of CO_2 on the catalysts, the CO_2 temperature-programmed desorption (CO_2-TPD) analysis was performed. The chemical desorption was performed at 10°C/min to 600°C.

Electrochemical measurements, In-situ Raman Spectroscopy, Density functional theory (DFT) calculations, and computational fluid dynamics CFD modelling are provided in the Supporting Information.

3. Results and discussion

3.1. Microstructure and morphology analysis

The fabrication strategy of defect-rich silver nanosheet-based hollow fiber gas-diffusion electrodes (D-AgNS HF) is illustrated in Fig. 1a. This process involves an initial galvanic replacement reaction (GRR) followed by controlled electrochemical oxidation and reduction to induce surface defects. To construct the HFGDEs, the bottom end of the hollow fiber is sealed, enabling CO_2 gas to be continuously fed through the open lumen, acting as a built-in gas chamber (Fig. 1a). The CO_2 gas then penetrates through the hollow fiber walls to reach the active sites. This continuous and localized CO_2 delivery is critical for maintaining high CO_2 availability at the reaction interface, thereby effectively suppressing the HER, especially under high current densities where rapid electron transfer intensifies competition between CO_2 and H_2O.

The difference in standard reduction potentials between Cu ($E^0_{Cu2+/Cu} = +0.34$ V) and Ag ($E^0_{Ag+/Ag} = +0.799$ V) enables the in-situ growth of a silver catalyst layer on the Cu substrate via GRR [31,32]. Achieving a robust and uniform silver catalyst layer on the Cu substrate requires a controlled GRR with a slow nucleation rate to promote the growth of smaller silver particles. In contrast, a rapid reaction rate results in loosely packed structures with larger silver particle sizes, compromising the mechanical and electrochemical stability of the electrode. For instance, direct immersion of Cu HF into $AgNO_3$ solution often results in the formation of a dendrite silver structure with poor adhesion [33,34].

For the first time, a silver ammonium solution was applied as the Ag^+ source for the galvanic replacement of copper with silver. The formation of the $Ag(NH_4)_2^+$ complex in solution effectively modulates the Ag^+ concentration, reducing the nucleation rate and enabling the growth of smaller silver particles on Cu HF. After a 2 h GRR process, the initial transparency of $Ag(NH_4)_2^+$ solution turned dark blue, while the Cu HF was converted into a white Ag HF (Figs. 1b, S2). The diameter of Ag HF is approximately 1.4 mm (Fig. 1c). The elemental mapping of cross-sectional Ag HF images (Fig. 1d) further confirmed that silver replacement occurred not only on the surface but also within the inner structure of the Cu HF. The amount of silver elements is more than 40.5 % (Figure S3), indicating a large amount of silver armoring on the Copper skeleton. EDS mapping of Ag HF (Figure S4a) and D-Ag NS HF (Figure S4b) further confirms that the electrode surface is fully covered with silver, with no detectable presence of copper. The cross-sectional SEM image of Ag HF revealed its porous structure (Figure S5a). Additionally, the smooth surface of Cu HF (Figure S3b) transformed into dense silver particles (Fig. 1e). Unlike previous methods that rely on

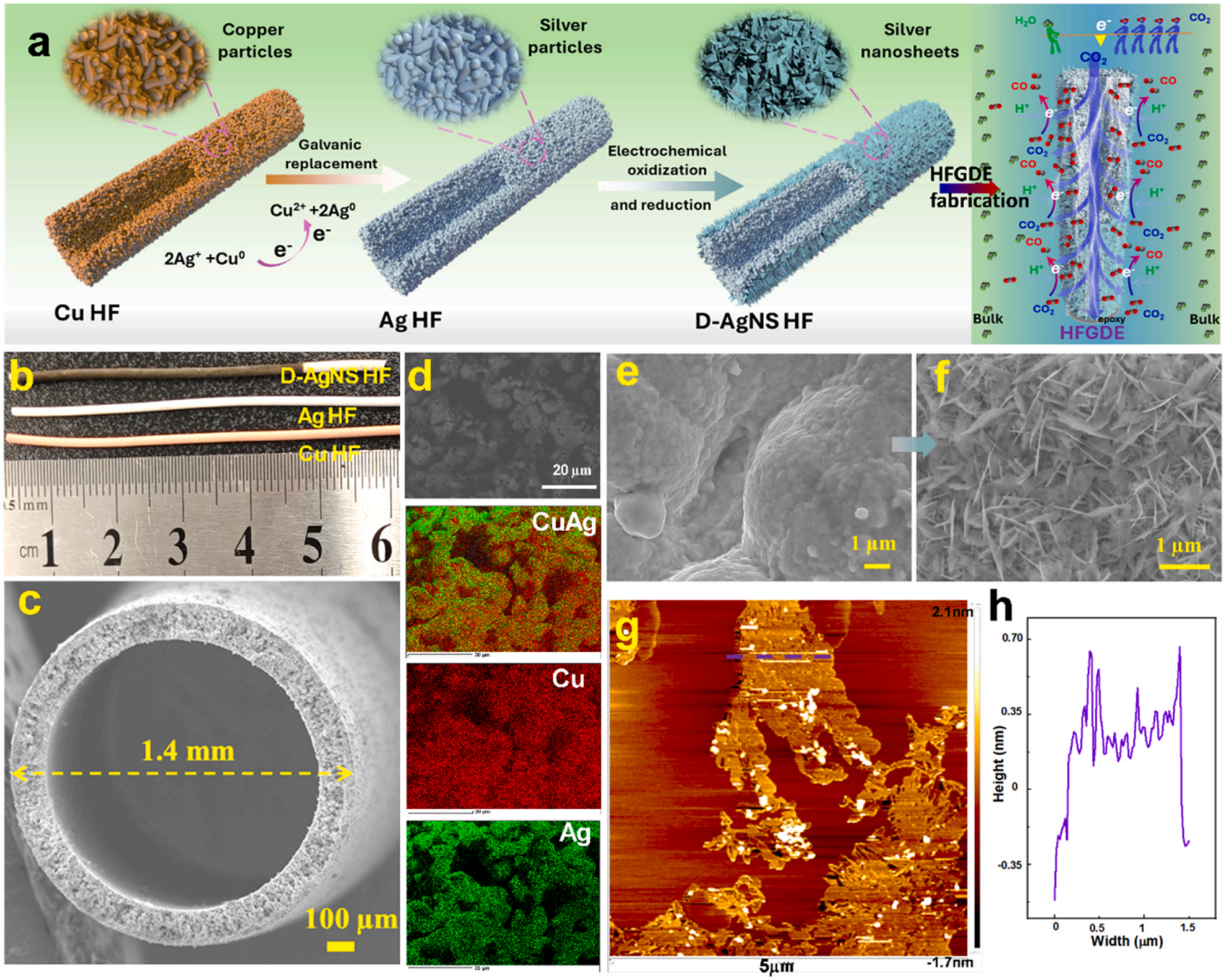

Fig. 1. a) Schematic illustration of fabricating defect-rich silver nanosheets-based hollow fiber electrodes; b) Photo images Cu HF, Ag HF, D-AgNS HF; c) Cross-sectional SEM image of Ag HF; d) EDS elemental mapping images of cross-sectional of Ag HF; Surface SEM images of e) Ag HF, and f) D-AgNS HF; g) Atomic force microscopy (AFM) image, and h) height profiles of silver nanosheets.

costly silver powders, we employ a cost-effective galvanic replacement strategy using Cu HFs as templates. Cu HFs can be readily fabricated at scale with high porosity and mechanical robustness, ensuring efficient CO_2 mass transfer. Their transformation into Ag HFs retains advantageous porous architecture while significantly lowering electrode production costs, offering a practical route for scalable CO_2 to CO electroreduction systems.

The growth of silver particles on Cu hollow fibers is governed not only by Ag^+ complexation but also by the reaction time during the galvanic replacement reaction. At 30 min of GRR, nanosized Ag particles were observed (Figure S5c). Continued reaction up to 2 h leads to further particle growth (Figure S5d), while prolonged reaction for 4 h results in the formation of bulk-phase silver, which blocks the porous structure of the hollow fibers (Figure S5e). The concentration of $[Ag(NH_3)_2]^+$ plays a critical role in regulating the availability of free Ag^+ ions. Using 0.02 M $[Ag(NH_3)_2]^+$ produces finer Ag nanoparticles (Figure S5f), indicating that Ag complexation slows the reaction rate by stabilizing Ag^+. In contrast, immersing Cu HFs directly into 0.1 M $AgNO_3$ for just 30 s results in the rapid deposition of bulky, dendritic silver structures (Figure S5g). Compared to Cu HF with abundant porous

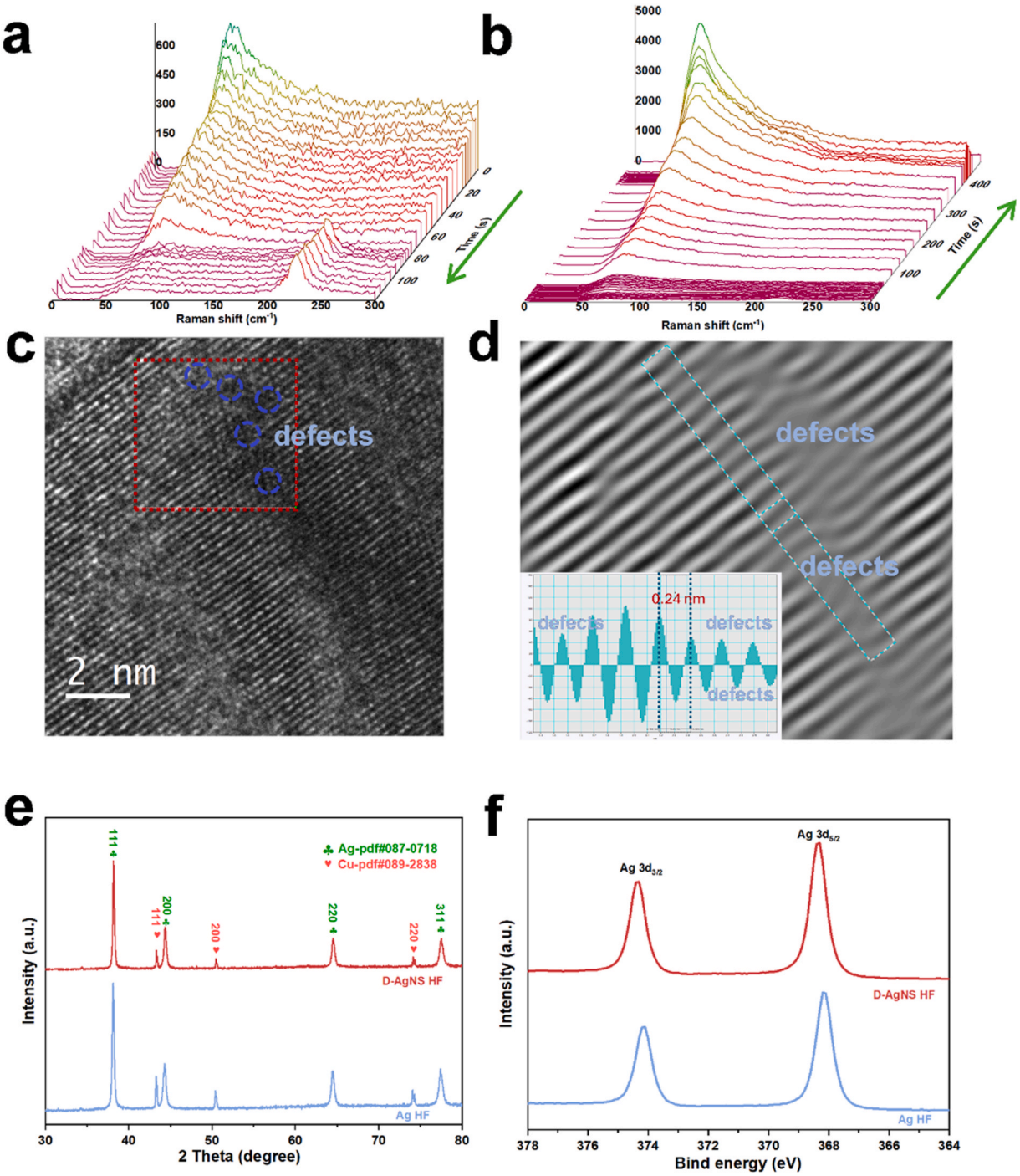

Fig. 2. Time-resolved operando Raman spectra of a) the oxidation of Ag HF, b) the reduction of oxidized Ag HF; c) High-resolution STEM image of D-AgNS HF; d) Inverse Fourier transform (IFFT) patterns of Ag (111) plane, corresponding to the red square area in c), the inserted picture is the line-scanning intensity profile of the green rectangle area in d); e) XRD patterns of Ag HF and D-AgNS HF; f) XPS spectra of Ag 3d for Ag HF and D-AgNS HF.

structures (Figure S5h), the Ag HF obtained after 2 h of GRR retains its porosity while exhibiting a higher density of deposited silver particles (Figure S5i).

The defect-rich silver nanosheet-based hollow fiber (D-AgNS HF) was subsequently prepared via in situ electro-oxidation and reduction of the Ag HF. The oxidation process was performed in 0.2 M NaOH with a single line sweep voltammetry (LSV) at a scanning rate of 5 mV/s, over a potential range of 0.2–0.8 (V vs. Ag/AgCl), revealing two distinct oxidation peaks (Figure S6a), corresponding to the formation of silver oxide. The SEM image of the outer surface of oxidized Ag HF revealed abundant cubic particles formed during the oxidation process (Figure S7a). The reduction of oxidized Ag HF was carried out in 0.5 M CO_2-saturated $KHCO_3$ at a constant current density of 5 mA/cm^2 for 600 s. The dense and thin silver nanosheet structure was observed from the surface SEM image of D-AgNS HF (Fig. 1f). Further AFM analysis confirmed that the silver nanosheets exhibited micron-scale lateral dimensions with a thickness of around 1–2 nm (Figs. 1g, 1h). These large and ultra-thin nanosheets significantly enhance the electrochemical surface area, facilitating efficient electrochemical conversion of CO_2.

The time-resolved operando Raman was applied to monitor the structural evolution of Ag HF during the oxidation and reduction process. The Raman peaks located at around 70 cm^{-1} and 220 cm^{-1} were attributed to the Ag-Ag bond and the Ag-O bond, respectively [35]. Interestingly, at the initial oxidation stage, not only the Ag-Ag Raman peak but also the overall Raman signal intensity decreased (Fig. 2a). The weakening in Raman signal intensity is attributed to the changed surface roughness of silver catalysts, as the rough silver particles could generate more hot spots to enhance the Raman signal [36]. Meanwhile, the formation of silver oxide also contributes to the reduction in Raman signal intensity. A distinct Ag-O Raman peak emerged at around 81 s of oxidation, corresponding to the potential of around 0.6 (V vs. Ag/AgCl) (Figure S6b). Simultaneously, the weakening of the Ag-Ag Raman peak indicated the transformation of metallic silver to silver oxide.

During the reduction process, the disappearance of the Ag-O Raman peak within the initial 20 s indicated the rapid reduction of surface silver oxide (Figure S8a). The Ag-Ag Raman intensity subsequently increased, reaching 2533 (a.u.) at 360 s and sharply rising to 5221 (a.u.) by 408 s (Fig. 2b), coinciding with a steep potential drop from −0.4 to −0.9 (V vs. Ag/AgCl) (Figure S6b). The observed sharp potential drop during the electroreduction process is attributed to the dynamic evolution of the electrode-electrolyte interface, accompanied by a reduction in charge-transfer resistance. The transformation of catalyst morphology and changes in surface energy likely enhance electron transfer. However, the Ag-Ag Raman peak intensity diminished due to the disturbance caused by the formation of hydrogen bubbles at more negative potentials (Figure S8b). After the 600 s reduction process and the removal of bubbles, the Raman intensity of D-AgNS HF was revealed to be slightly lower than the maximum observed at 408 s but over four times higher than that of pristine Ag HF (Figure S9), indicating a significantly enhanced surface roughness of silver catalysts.

To further illustrate the growth mechanism of defect-rich silver nanosheets, SEM images were captured at different growth intervals (Figure S7). During the initial 30 s, the rapid reduction of surface Ag_2O led to the formation of smaller sizes of silver particles (Figure S7b). From 31–360 s, a progressive increase in surface roughness was observed, marking the onset of nanosheet structure formation (Figure S7c). Lastly, a pronounced increase in surface roughness occurred at the time range from 361 to 420 s, accompanied by a significant potential drop, facilitating the formation of a 2D nanosheet structure (Figure S7d).

The reduction from Ag_2O to Ag is usually accompanied by volume contraction and the cleavage of Ag-O bonds, leading to the loss of Ag atoms and the formation of lattice defects [21]. High-resolution TEM has been proven to be an effective characterization technique for identifying the existence of lattice defects [22]. The distinct absence of silver atoms was observed in Fig. 2c, indicating the existence of lattice defects. The line-scanning intensity profile in Fig. 2d further confirmed that these vacancies correspond to Ag vacancies in the Ag (111) crystal plane. Similar defect patterns have been observed in the bismuth nanosheets and silver catalysts [21,22]. This may be due to the formation of Ag-Ag bonds accompanied by the breaking of Ag-O bonds. Furthermore, the reduction from Ag_2O to Ag is accompanied by the reduction of volume, which may lead to the loss of Ag atoms, thus leading to the formation of defects. The abundant defects could provide more active sites to accelerate charge transfer and improve the catalytic activity [37]. In contrast, the pristine Ag HF exhibited a perfect lattice structure corresponding to the Ag (111) crystal plane, indicating the absence of such defect structures (Figure S10).

The crystal microstructure of Ag HF and D-AgNS HF was further characterized via X-ray diffraction (XRD), and four distinct peaks of 2-theta at 38.2, 44.3, 64.4, 77.5° were observed from Fig. 2e, corresponding to the Ag (111), (200), (220), and (311) crystal planes of Ag phase (PDF#87–0718). The weak background Cu peaks of Cu (111), (200), and (220) were also observed. The surface electronic states and elemental composition of Ag HF and D-AgNS HF were investigated using X-ray photoelectron spectroscopy (XPS). The Ag 3d spectra exhibit two prominent peaks at approximately 374.3 and 368.3 eV, corresponding to the Ag $3d_{3/2}$ and Ag $3d_{5/2}$ core levels, respectively, characteristic of metallic Ag^0 (Fig. 2f). Notably, the D-AgNS HF sample shows a subtle positive shift of + 0.15 eV in binding energy relative to Ag HF. This shift is attributed to under-coordinated Ag atoms, likely arising from defect-induced electron localization, consistent with previous reports [18,38]. The presence of Ag-vacancy defects is further corroborated by near-edge X-ray absorption fine structure spectroscopy (NEXAFS) analysis. In particular, a positive shift in the Ag M_5-edge position was observed for D-AgNS HF (Figure S11), further supporting its defect-rich character.

As shown in the Ag M_5-edge NEXAFS spectra (Figure S11), both Ag HF and D-AgNS HF exhibit spectral line shapes closely resembling that of a metallic Ag foil, confirming the predominance of Ag^0 in both samples. However, D-AgNS HF shows a minor shift (~0.15–0.20 eV) of the absorption threshold toward higher photon energy. This subtle edge shift is indicative of under-coordinated or vacancy-rich Ag sites, where a reduced 4d/5 s electron density leads to diminished final-state screening, resulting in a slight increase in the apparent absorption edge energy [39,40]. The absence of a larger displacement corroborates that the Ag lattice remains metallic, with only localized electronic perturbations induced by the defects.

3.2. *Catalyst activity dominates CO_2 to CO electroreduction at low current density*

The electrocatalytic performance of Ag HF and D-AgNS HF for converting CO_2 to CO was evaluated in a customized H-cell at a wide potential range from −0.4 to −1.2 (V vs. RHE) using 0.5 M KCl as catholyte. The D-AgNS HF electrode demonstrated superior intrinsic selectivity for CO production, achieving over more than 90 % FE for CO across a potential range from −0.6 to −1.1 (V vs. RHE), compared to the Ag HF (Fig. 3a). Notably, the D-AgNS HF reached a peak CO FE of 93.5 % at −0.8 (V vs. RHE). The higher selectivity for CO and lower selectivity for H_2 formation (Fig. 3b) over D-AgNS HF indicate the higher CO_2RR activity over defect-rich silver nanosheets. The partial current densities of CO (PCD_{CO}) for both electrodes increased with moving to more negative potentials, reflecting their excellent electron transfer properties between electrodes and in situ grown silver catalysts. The D-AgNS HF consistently exhibited a higher PCD_{CO}, reaching 85.1 mA/cm^2 at −1.2 (V vs. RHE), significantly outperforming Ag HF, which achieved only 64.8 mA/cm^2 under the same conditions (Fig. 3c). The Cu HF exhibited a strong preference for formate production (Figure S12), achieving a FE of approximately 70 % over the potential range of −1.0 to −1.3 V (vs. RHE). In contrast, no liquid-phase products were detected for either the Ag HF or D-AgNS HF electrodes. This absence of formate formation confirms that the underlying Cu skeleton, fully covered by the Ag catalyst layer, did not participate in the

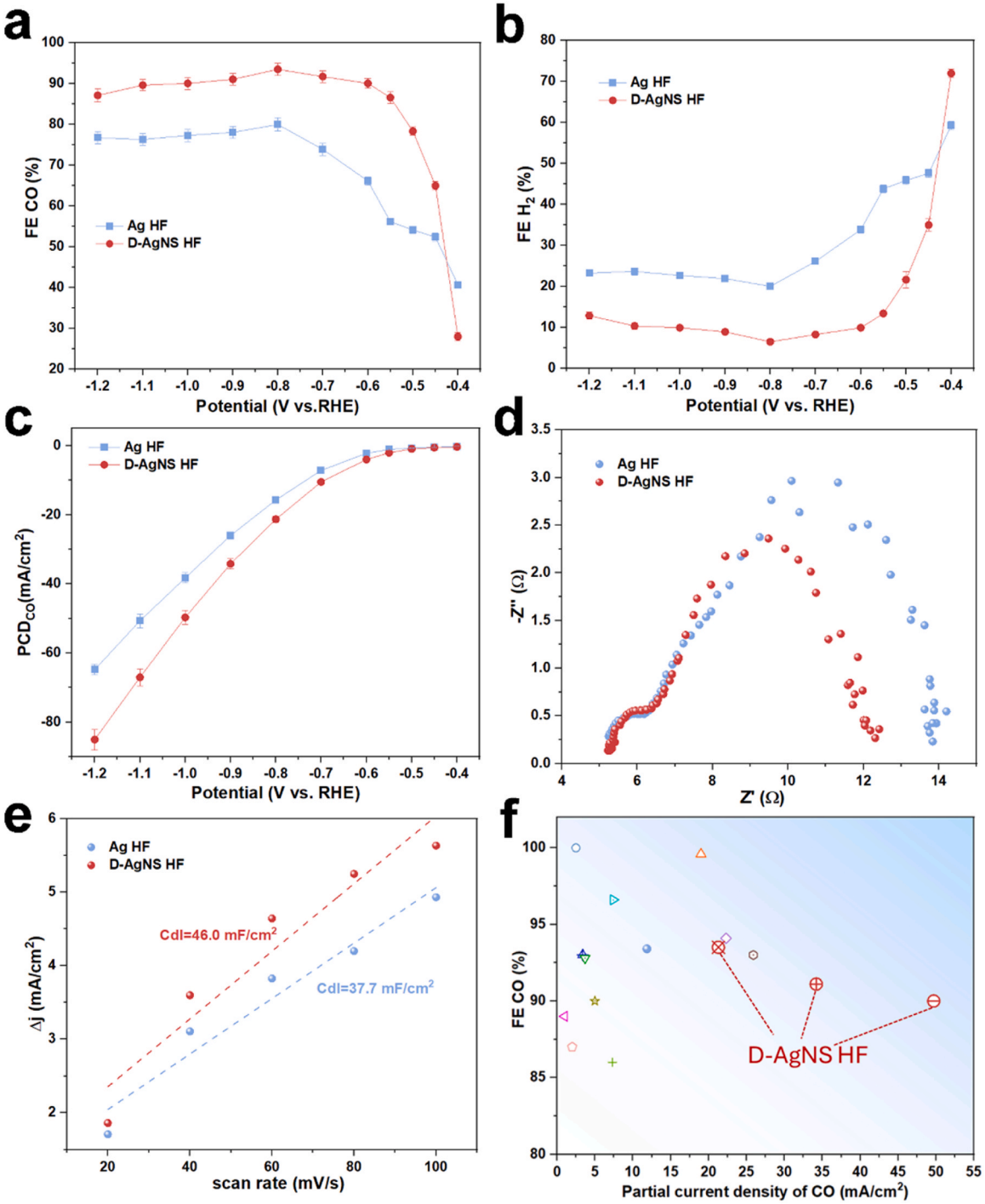

Fig. 3. a) Faradaic efficiency of CO, and b) H_2 for HFGDEs; c) Partial current density of CO over HFGDEs; d) Electrochemical impedance spectroscopy (EIS) Nyquist plot over HFGDEs; e) Dual-layer capacitance (Cdl) values over HFGDEs; f) Comparison of the CO_2RR performance for the state-of-the-art Ag-based electrocatalysts.

electrochemical reaction.

The superior catalytic performance of D-AgNS HF is attributed to the rich defects within silver nanosheets, providing fast electron transfer and enriched active sites. Electrochemical impedance spectroscopy (EIS) measurements at −0.8 (V vs. RHE) revealed a lower charge transfer resistance of 7.0 Ω for D-AgNS HF, indicating improved electron transfer kinetics (Fig. 3d). Double-layer capacitance (Cdl) measurements further supported the enhanced electrochemically active surface area (ECSA) of D-AgNS HF electrode, exhibiting a higher Cdl of 46.0 mF/cm^2 compared to 37.7 mF/cm^2 of Ag HF (Fig. 3e).

The overall electrocatalytic performance is determined not only by the intrinsic activity and active site density but also by the CO_2 availability at the catalytic sites. While state-of-the-art silver-based electrocatalysts exhibit excellent Faradaic efficiencies at low current densities, their performance typically declines significantly under high current density conditions in a H-Cell setup [41]. In contrast, the D-AgNS HF delivered a high current density and maintained a high Faradaic efficiency (over 90 %) for CO production (Fig. 3f, Table S1). This is attributed to the flow-through GDE configuration, forcing the gas penetrating through the hollow fiber walls and ensuring sufficient CO_2 near the catalytic sites, which differs from electrocatalysts coupled with conventional planar or porous electrodes, where the CO_2 supply is

limited from dissolved CO_2 in the bulk electrolytes, compromising their performance at higher current densities.

3.3. Mechanisms study on CO_2RR activity of the D-AgNS HF

To further elucidate the intrinsic properties and defect contribution of the D-AgNS HF electrode on CO_2 electrochemical reduction, the partial current density of CO was normalized by ECSA and presented in Figure S13. The higher normalized PCD_{CO} observed for the D-AgNS HF electrode indicates the enhanced intrinsic catalytic activity, demonstrating that ECSA is not the sole contributor to its outstanding CO_2RR performance. The Tafel analysis was conducted to investigate the CO_2RR kinetics of Ag HF and D-AgNS HF electrodes. In general, a Tafel slope of 118 mV/dec suggests that the reaction-determining step (RDS) is the

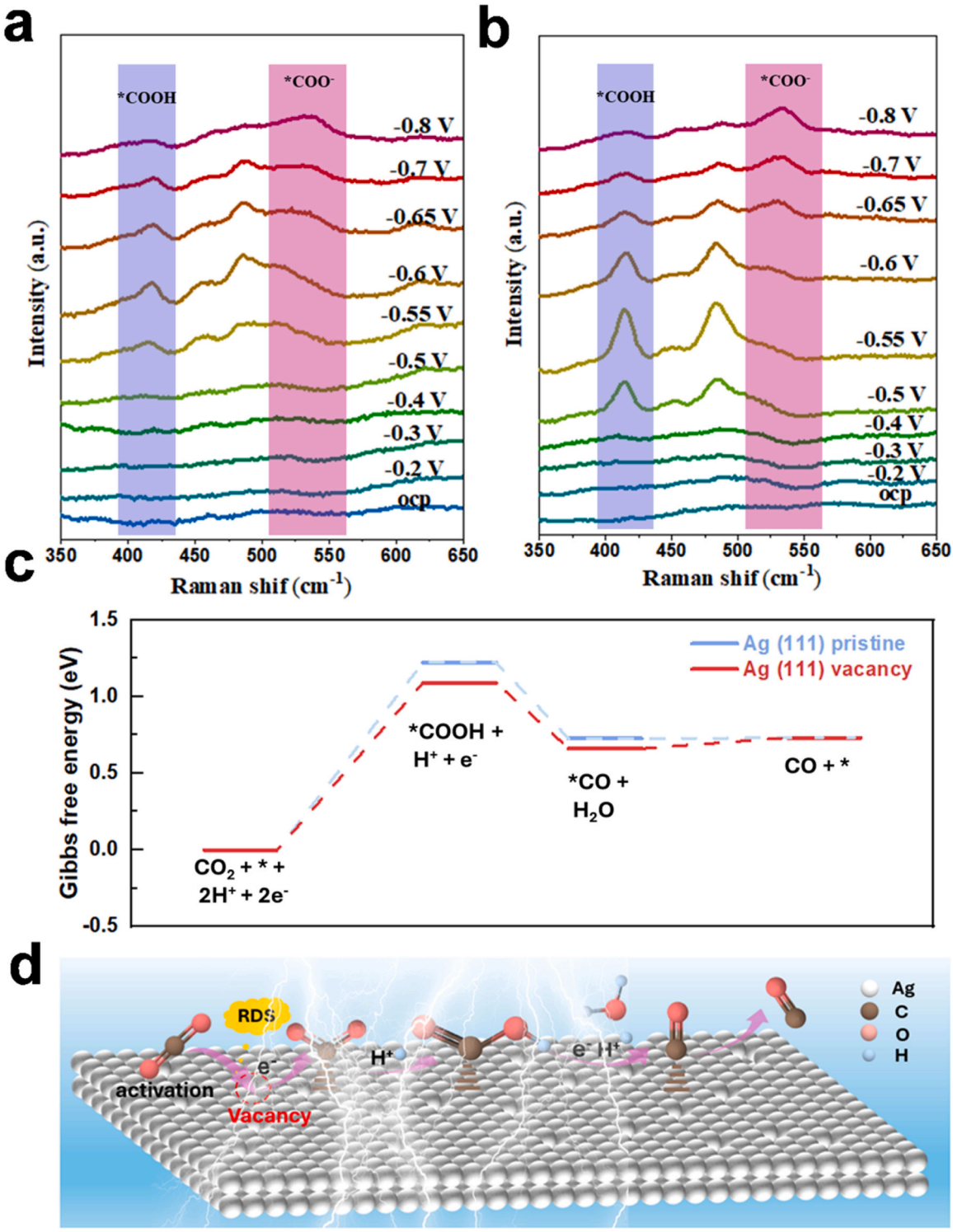

Fig. 4. Time-resolved operando Raman spectra to monitor CO_2RR intermediates at applied potentials over a) Ag HF, and b) D-AgNS HF electrodes. c) Calculated free energy of CO formation on Ag (111) pristine and Ag (111) vacancy; d) Proposed reaction pathway for electrochemical reduction CO_2 to CO on the D-AgNS HF electrode surface.

one-electron transfer step to form *COO^- intermediate, and a lower Tafel slope value implies more favorable reaction kinetics [42]. The D-AgNS-HF electrode exhibited a Tafel slope of approximately 142 mV/dec, approaching the theoretical value of 118 mV/dec and significantly lower than that of Ag HF (216 mV/dec), indicating fast reaction kinetics derived from defect-rich silver nanosheets (Figure S14).

The formation of vacancies and charge accumulation from defect-rich silver nanosheets can enhance the adsorption of the CO_2 molecules and reaction intermediates, thereby facilitating the reaction kinetics [21,37]. Temperature-programmed desorption (TPD) of CO_2 was performed to investigate the adsorption capability of CO_2 molecules over Ag HF and D-AgNS HF electrodes. The CO_2 desorption peak shifts toward higher temperature from 403 °C of Ag HF to 456 °C of D-AgNS HF, indicating an increment of CO_2 binding strength on the defect-rich silver nanosheets (Figure S15) [43]. Moreover, the adsorption behavior of the *COO^- intermediate on the electrodes was inferred using OH^- working as a proxy in N_2-saturated 0.1 M KOH via a single oxidative LSV scan (Figure S16) [44]. The D-AgNS HF exhibited a lower potential for OH^- adsorption, suggesting the stronger *COO^- binding, which stabilizes *COO^- intermediates and accelerates the CO_2RR kinetics.

The potential-related in-situ Raman spectroscopy was utilized to further investigate the CO_2RR mechanism on Ag HF and D-AgNS HF electrodes. As revealed by Fig. 4a and b, two characteristic Raman peaks were located at around 410 cm^{-1} and 528 cm^{-1}, corresponding to adsorbed *COOH and *COO^- intermediates on the electrode surface [45]. They are key intermediates for the electrochemical conversion of CO_2 to CO. The Raman peak observed at 480 cm^{-1} may correspond to adsorbed *CO intermediates on the catalyst surface. The peak intensity of *COOH and *COO^- increased at more negative potentials, reflecting higher surface adsorption of intermediates consistent with the observed CO_2RR activity trend (Fig. 3c). Notably, the *COOH peak was detected on the D-AgNS-HF at a lower potential of −0.5 (V vs. RHE), and the intensities of both *COOH and *COO^- peaks were significantly higher than those for Ag HF, demonstrating the superior activity of defect-rich silver nanosheets for CO_2 activation and conversion. The observed decrease in Raman intensity of *COOH and *COO^- for both electrodes after −0.6 V (vs. RHE) is attributed to the interference caused by H_2 bubble formation at the electrode-electrolyte interface. These in-situ Raman results provide direct experimental evidence supporting the enhanced CO_2 activation kinetics facilitated by defect-rich silver nanosheets, in agreement with the above Tafel analysis, CO_2-TPD, oxidative LSV, and CO_2RR performance data.

Density functional theory (DFT) calculations were performed to investigate the energetics of the key intermediates (*COOH and *CO) involved in the CO_2RR to CO on silver catalysts. The Ag (111) crystal facet was selected as a representative model for the DFT calculations, despite the presence of other Ag crystal facets (e.g., Ag (200), Ag (220), and Ag (311)) observed in the XRD pattern, which is based on both experimental evidence and prior literature. High-resolution STEM images of D-AgNS HF (Fig. 2c) and Ag HF (Figure S10) reveal that the lattice distance of 0.24 nm corresponds to the Ag (111) plane. This observation is further supported by the dominant intensity of the Ag (111) diffraction peak at 38.2° in the XRD pattern. Furthermore, the Ag (111) surface has been widely adopted in literature as a model facet for investigating CO_2 reduction, particularly for evaluating the adsorption behavior of key intermediates such as *COO^- and *COOH [17,21]. A perfect Ag (111)-pristine slab mode was constructed to simulate the intact Ag structure in pristine Ag HF, and the Ag (111)-vacancy slab mode was built by removing one Ag atom from the perfect Ag (111) slab to simulate the defect-rich silver nanosheets in D-AgNS HF. Adsorption energy (ΔE_{ads}) calculations were conducted at four high-symmetry sites (top site, fcc hollow site, hcp hollow site, and bridge site) for both *COOH and *CO on Ag (111)-pristine and Ag (111)-vacancy surfaces. These results, summarized in Table S2, identified the top site as the most favorable adsorption site for both intermediates (Figure S17). Specifically, the ΔE_{ads} of COOH on Ag (111)-vacancy was −2.05 eV, lower than −1.99 eV of Ag (111)-pristine (Figure S18), indicating stronger binding on the vacancy-rich surface. These findings align with in-situ Raman spectroscopy results (Fig. 4a, b), which also demonstrated enhanced intermediate binding on defect-rich silver nanosheets.

In addition, the calculated Gibbs free energies (ΔG) for *COOH and *CO formation on the Ag (111)-pristine surface were 1.22 and 0.72 eV, respectively (Fig. 4c). In terms of Ag (111)-vacancy surface, the ΔG for producing *COOH and *CO was significantly reduced to 1.09 and 0.66 eV, respectively (Fig. 4c). These results indicate that the Ag (111)-vacancy surface is more energy favorable to facilitate the electrochemical reduction of CO_2 to CO by significantly reducing the energy barrier for key intermediates formation. Based on the above experiments and DFT calculations, a proposed mechanism for CO_2RR to CO on the D-AgNS HF electrodes is illustrated in Fig. 4d. The reaction begins with CO_2 activation on the Ag (111)-vacancy surface to form the *COO^- intermediate, which is identified as the rate-determining step. The *COO^- intermediate reacts with a proton to form *COOH intermediate, which subsequently undergoes further proton-coupled electron transfer to generate H_2O and *CO. Finally, *CO desorbs from the electrode to release CO, leaving the active sites open for the next catalytic cycle.

3.4. CO_2 availability dominates CO_2 to CO electroreduction at high current density

It is arguably that the intrinsic activity and the number of catalytic sites primarily contribute to the CO_2RR activity at low current densities. However, at high current densities, the rapid consumption of CO_2 can deplete CO_2 availability near the active sites, favoring the undesired HER and diminishing CO_2RR activity [23,24,41]. Therefore, ensuring sufficient CO_2 availability becomes critical for suppressing HER and sustaining high CO_2RR efficiency under high current densities. The flow-through GDE mode addresses this challenge by continuously delivering convective CO_2 to the catalytic sites, significantly enhancing mass transport and providing superior CO_2 availability at the triple-phase interfaces.

When operated in flow-through GDE mode (Figs. 5a, S19a), CO_2 is fed through the lumen side of the hollow fiber electrode, with the bottom end sealed by epoxy, enabling CO_2 to penetrate through the hollow fiber walls and reach the catalyst/electrolyte interfaces. This will introduce turbulent flow near the pore structure, accelerating mass transfer and facilitating reaction kinetics [46,47]. The GDE configuration requires the CO_2 to overcome the capillary pressure of the micron-scale pore structure, achieving adequate gas flow through the fiber walls [25]. The computational fluid dynamics (CFD) modeling visualized the CO_2 distribution on D-AgNS HF in GDE mode (Fig. 5b), where the CO_2 continuously flows through the hollow fiber micron-scale channels, efficiently reaching the catalyst-electrolyte interfaces. In contrast, under non-GDE mode, CO_2 gas is bubbled directly into the catholyte, resulting in negligible CO_2 pressure and a flooded pore structure in the hollow fiber electrodes (Figs. 5c, S19b). The CO_2 mass transportation is hindered by the long diffusion path from the bulk electrolytes to the catalytic sites, significantly impairing CO_2RR performance (Fig. 5d).

A chloride-containing electrolyte (e.g., KCl) has been reported to suppress HER and promote the electroreduction of CO_2 to CO. However, using KCl alone at high current density might lead to the alkalization of catholyte, which may cause salt precipitation and reduced product selectivity. To address this issue, we investigated the effect of $KHCO_3$ buffer concentration on CO selectivity over the D-AgNS HF electrode (Figure S20). When 0.1 M $KHCO_3$ was added to 1 M KCl, the CO selectivity slightly decreased to 84.3. However, a further increase to 1 M $KHCO_3$ led to a significant drop in CO selectivity to 65.2 under a current density of 200 mA/cm^2. Based on this, 1 M KCl with 0.1 M $KHCO_3$ was selected as the optimal catholyte, as it maintained a pH of 6.8 after 30 min of electrolysis under 200 mA/cm^2. At high current densities, to

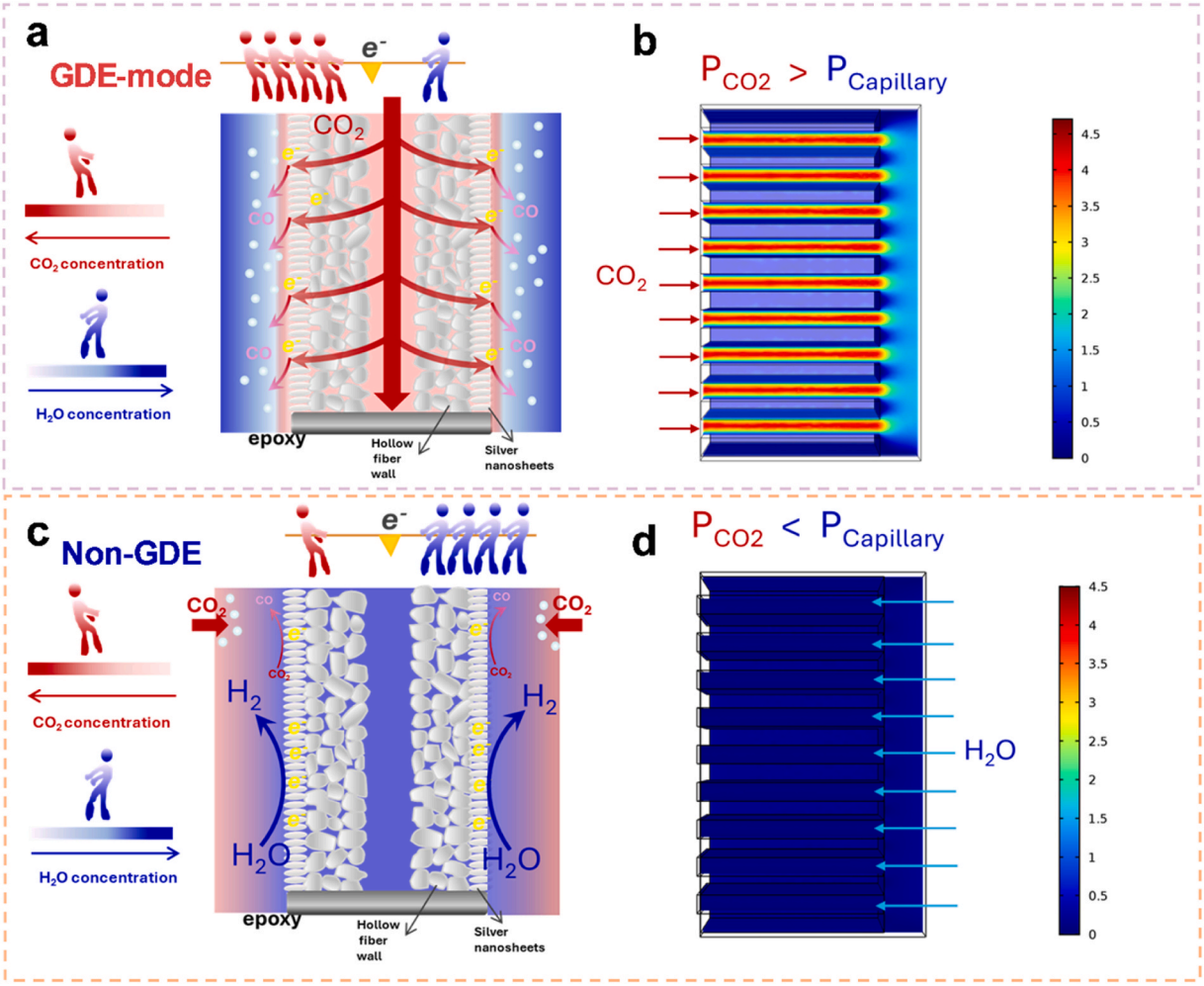

Fig. 5. a) Schematic illustration, and b) Computational fluid dynamic (CFD) modeling of the CO_2 and water distribution on D-AgNS HF in GDE mode, the red to blue color suggests the reduce of CO_2 velocity; c) schematic illustration, and d) CFD modelling of the CO_2 and water distribution on D-AgNS HF in non-GDE mode, the blue color suggests the water flooding.

fight for electrons, a tug-of-war between CO_2 and water intensifies. CO_2 can win the flag to promote CO_2 conversion if there is a sufficient gas supply from electrodes (Fig. 5a). Otherwise, the HER becomes the dominant reaction pathway (Fig. 5c). This is evident in the Faradaic efficiency of CO (FE CO) over hollow fiber electrodes operated in GDE and non-GDE modes (Fig. 6a). For the D-AgNS HF performed in non-GDE mode, FE CO sharply reduced to 34.5 % at 100 mA/cm^2, and further dropped to 16.8 % at 500 mA/cm^2. In contrast, under GDE mode, the D-AgNS HF electrode maintained significantly higher FE CO values of 89.7 % and 74.4 % at the same current densities, respectively. In terms of H_2 formation, both Ag HF and D-AgNS HF electrodes in GDE mode exhibited a lower Faradaic efficiency of H_2 below 41 % while exhibiting significantly higher FE of H_2 above 82 % under non-GDE mode (Figure S21). Under non-GDE and low applied potentials, the Ag HF and D-Ag NS HF electrodes exhibited increasing FE CO with applying more negative potentials (Figure S22), in contrast to the sharp decline of FE CO (Fig. 6a) observed under high current densities (50–500 mA/cm^2). The D-AgNS HF (non-GDE) reached a peak FE CO of 84.9 % at −0.9 V (vs. RHE) and a higher PCD_{CO} of 11.5 mA/cm^2 at −1.0 V (vs. RHE) (Figures S22, 23). These results indicate that at low current densities (potentials), CO_2 availability is not the limiting factor for the CO_2 to CO electroreduction, but rather catalyst activity.

In GDE mode, the D-AgNS HF electrode achieved a PCD_{CO} as high as 381.8 mA/cm^2 and a CO production rate of 6935.3 μmol/h•cm^2, compared to only 84.1 mA/cm^2 and 1568.1 μmol/h•cm^2 in non-GDE mode (Figs. 6b, 6c). Moreover, the ratio of PCD_{CO} in GDE to non-GDE mode exhibited a significant increase with current density, rising from 1.35 at 50 mA/cm^2 to 2.6 at 100 mA/cm^2, further to 4.42 at 500 mA/cm^2 for the D-AgNS HF electrode. Similarly, the ratio for the Ag HF also increased sharply from 1.27 at 50 mA/cm^2 to 4.36 at 500 mA/cm^2 (Fig. 6d). These results highlight that, compared to the intrinsic activity of the electrocatalysts, a sufficient CO_2 supply enabled by the flow-through GDE configuration is more critical to winning the electrons at high current densities, thereby suppressing HER and maintaining CO_2RR activity.

The long-term stability testing of both electrodes was carried out in a customized flow cell (Figure S24) with 1 M KCl (0.1 M $KHCO_3$) as the catholyte at an industrial-level current density of 300 mA/cm^2. The D-AgNS HF electrode demonstrated excellent stability (Fig. 6e), maintaining a FE CO around 80 % during 48 h of continuous operation at 300 mA/cm^2. The Ag HF electrode also exhibited stability exceeding 24 h (Figure S25), suggesting the robust performance of the hollow fiber gas diffusion electrode configuration. Post-stability XRD analysis confirmed the structural integrity of Ag crystal facets in both electrodes (Figure S26). The SEM image of the D-AgNS HF electrode surface revealed the preserved silver nanosheet structure (Figure S27a), while small particles emerged on the Ag HF electrode after stability (Figure S27b). The obvious K signal concentration in the cross-section of Ag HF (Figure S28) indicates the formation of carbonate precipitation during the stability test, which will not only block the gas diffusion

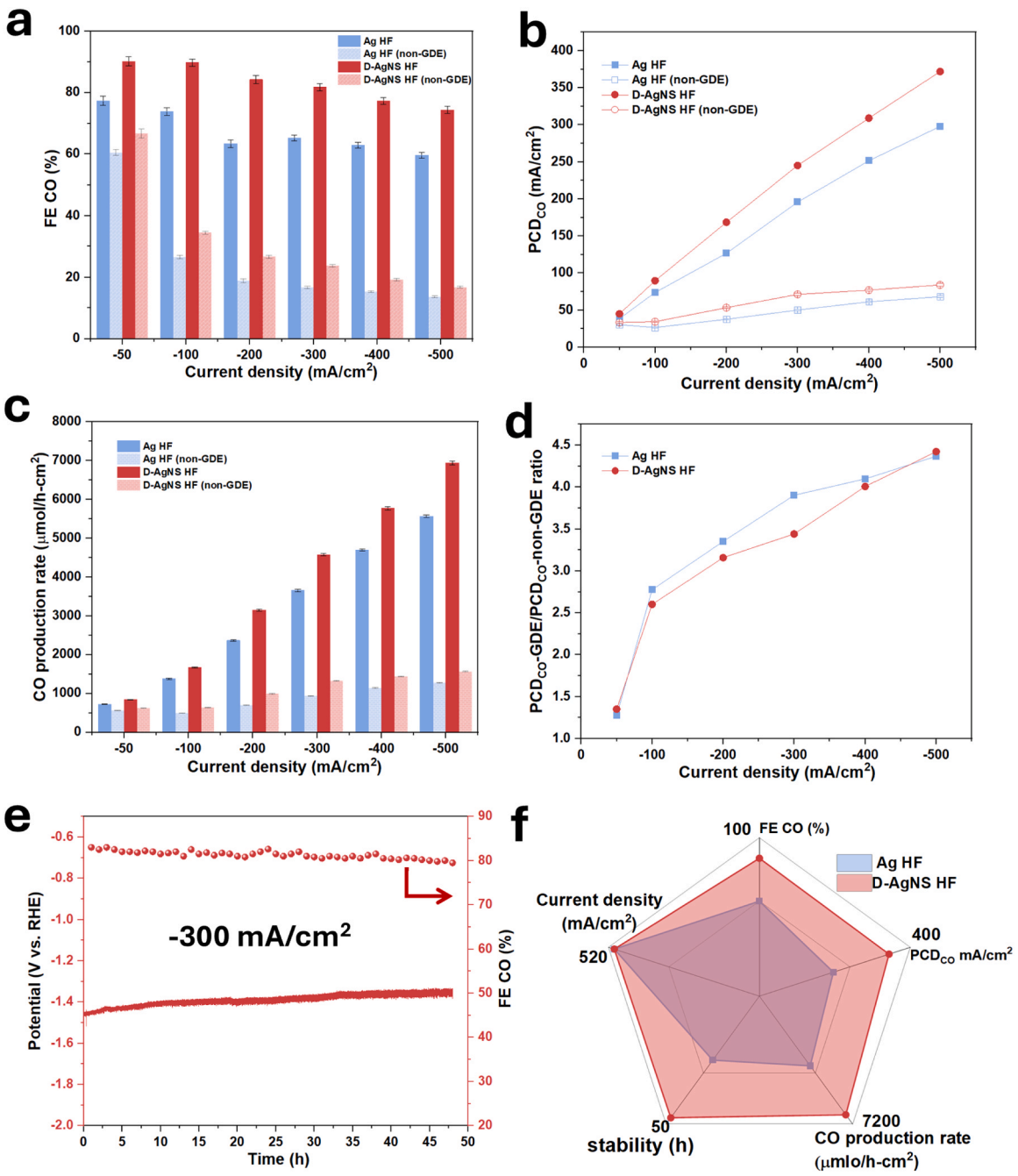

Fig. 6. a) Faradaic efficiency of CO, b) Partial current density of CO (PCD_{CO}), and c) production rate of CO for Ag HF and D-AgNS HF electrodes performed in GDE and non-GDE mode at applied current densities; d) the ratio of PCD_{CO}-GDE/PCD_{CO}-non-GDE for Ag HF and D-AgNS HF electrodes; e) long-term operation of D-AgNS HF electrode in customized flow cell at −300 mA/cm^2; f) Overall CO_2RR performance comparison for Ag HF and D-AgNS HF electrodes.

channel but also cover the active sites. Furthermore, the water contact angle of the Ag HF electrode (Figure S29) decreased significantly from 84.2 to 32.2°, confirming that the hygroscopic nature of the salt leads to increased surface hydrophilicity, contributing to a decline in catalytic activity. The comparison with state-of-the-art electrocatalysts for CO production further highlights the superior performance of the D-Ag NS HF electrode (Table S3). The D-AgNS-HF electrode achieved a higher FE CO of 93.5 % at −0.8 (V vs. RHE), coupled with a higher PCD_{CO} and CO production rate (Fig. 6f). This outstanding performance is attributed to the synergistic effect of its defect-rich silver nanosheets and flow-through GDE configuration, which ensures efficient CO_2 delivery to the highly active catalytic sites.

4. Conclusion

In this study, we engineered a hollow fiber gas-diffusion electrode with in-situ grown, defect-rich silver nanosheets to systematically investigate the relative influence of catalyst activity and CO_2 availability on CO_2 to CO electroreduction across current densities up to 500 mA/cm^2. High-resolution STEM and operando Raman spectroscopy confirmed the formation of Ag (111) crystal plane defect sites during electrochemical reduction, evidenced by a sharp potential drop and enhanced Raman signal intensity. At low current densities, CO_2RR performance is primarily governed by the intrinsic activity of the catalyst. The abundant defect sites in the silver nanosheets promote CO production by stabilizing the *COOH intermediate, as supported by in-

situ Raman spectroscopy and DFT calculations, leading to a high Faradaic efficiency of CO of 93.5 % at −0.8 (V vs. RHE). However, as current density increases toward industrially relevant levels, CO_2 availability becomes the limiting factor. Crucially, experimental results combined with CFD modeling revealed that the competition between CO_2 and H_2O for electrons intensifies at high current densities. The sharply increasing ratio of the partial current density of CO in GDE versus non-GDE mode highlights the dominant role of CO_2 availability in sustaining CO_2RR and suppressing HER under such conditions. The D-AgNS HF electrode achieved a partial current density of CO of 381.8 mA/cm^2 under a total current density of 500 mA/cm^2, attributed to the HFGDE configuration ensuring sufficient CO_2 delivery to the active sites. In summary, while catalyst activity dominates at low current densities, CO_2 availability becomes the decisive factor at industrially relevant current densities. This work highlights a promising strategy for the rational design of flow-through gas diffusion electrodes to maximize desired conversion under industrially relevant conditions. The tunable porosity, tailored catalyst loading, and gas flow configuration make hollow fiber promising for targeting other CO_2RR production (e.g., formate, ethanol) or other gas-phase reactions (e.g., electroreduction of N_2, CO). However, achieving uniform pore size distribution during hollow fiber fabrication remains a significant challenge. Controlling pore uniformity is critical to ensure consistent gas permeability and to maximize the proportion of open pores for efficient gas transport and reaction accessibility.

CRediT authorship contribution statement

Guoliang Chen: Conceptualization, Data curation, Investigation, Formal analysis, Validation, Writing-original draft, Writing- review & editing. **Min Hong:** DFT calculation, Investigation. **Beibei Ma:** Data curation, Investigation. **Yizhu Kuang:** Data curation, Investigation. **Hesamoddin Rabiee:** Investigation, Methodology, Validation, Writing-review & editing. **Xiaomin Xu:** Data curation, Investigation. **Fatereh Dorosti:** Investigation, Formal analysis. **Penghui Yan:** Data curation, Investigation. **Nilam Shah:** Data curation, Investigation. **Ashok Kumar Nanjundan:** Validation, Writing- review & editing. **Zhonghua Zhu:** Project administration, Resource, Writing- review & editing. **Hao Wang:** Project administration, Funding acquisition, Validation, Methodology, Supervision, Resource, Writing- review & editing. **Lei Ge:** Conceptualization, Methodology, Supervision, Validation, Funding acquisition, Resource, Writing- review & editing.

Declaration of Competing Interest

The authors declare that they have no known competing financial interests or personal relationships that could have appeared to influence the work reported in this paper.

Acknowledgements

We acknowledge financial support from the ARC Future Fellowship (FT220100166), Discovery project (DP190101782) and Centre of Excellence for Green Electrochemical Transformation of Carbon Dioxide (CE230100017). Dr Hesamoddin Rabiee acknowledges SNSF Swiss Postdoctoral Fellowship (217305). NEXAFS measurements were carried out on the Soft X-ray Spectroscopy beamline at the Australian Synchrotron, ANSTO. We are grateful for the technical support from Lars Thomsen of the Australian Synchrotron, ANSTO.

Appendix A. Supporting information

Supplementary data associated with this article can be found in the online version at doi:10.1016/j.apcatb.2025.125902.

Data Availability

Data will be made available on request.

References

[1] P. De Luna, C. Hahn, D. Higgins, S.A. Jaffer, T.F. Jaramillo, E.H. Sargent, What would it take for renewably powered electrosynthesis to displace petrochemical processes? Science 364 (2019) eaav3506.
[2] R.S. Haszeldine, Carbon capture and storage: how Green can black be? Science 325 (2009) 1647–1652.
[3] F.P. García de Arquer, C.-T. Dinh, A. Ozden, J. Wicks, C. McCallum, A.R. Kirmani, D.-H. Nam, C. Gabardo, A. Seifitokaldani, X. Wang, CO_2 electrolysis to multicarbon products at activities greater than 1 a cm^{-2}, Science 367 (2020) 661–666.
[4] W.J. Teh, M.J. Kolb, F. Calle-Vallejo, B.S. Yeo, Enhanced charge transfer kinetics for the electroreduction of carbon dioxide on silver electrodes functionalized with cationic surfactants, Adv. Funct. Mater. 33 (2022) 2210617.
[5] Y. Liu, Z. Wei, X. Su, X. Shi, L. Liu, T. Wang, X. Xu, M. Zhao, Y. Zhai, H.B. Yang, B. Liu, Promoting electrochemical CO_2 reduction to formate via Sulfur-Assisted electrolysis, Adv. Funct. Mater. (2024) 2403547.
[6] H. Rabiee, B. Ma, Y. Yang, F. Li, P. Yan, Y. Wu, X. Zhang, S. Hu, H. Wang, L. Ge, Z. Zhu, Advances and challenges of Carbon-Free Gas-Diffusion electrodes (GDEs) for electrochemical CO_2 reduction, Adv. Funct. Mater. 35 (2024) 2411195.
[7] J.E. Huang, F. Li, A. Ozden, A. Sedighian Rasouli, F.P. García de Arquer, S. Liu, S. Zhang, M. Luo, X. Wang, Y. Lum, CO_2 electrolysis to multicarbon products in strong acid, Science 372 (2021) 1074–1078.
[8] L. Zhan, Y. Wang, M. Liu, X. Zhao, D. Deng, X. Zheng, J. Jiang, X. Xiong, Y. Lei, Chin. Chem. Lett. 36 (2025) 109695.
[9] Y. Zhao, X. Liu, Z. Liu, X. Lin, J. Lan, Y. Zhang, Y.R. Lu, M. Peng, T.S. Chan, Y. Tan, Spontaneously Sn-Doped Bi/BiO_x Core-Shell nanowires toward High-Performance CO_2 electroreduction to liquid fuel, Nano Lett. 21 (2021) 6907–6913.
[10] M. Liu, L. Zhan, Y. Wang, X. Zhao, J. Wu, D. Deng, J. Jiang, X. Zheng, Y. Lei, Achieving integrated capture and reduction of CO_2: a promising electrocatalyst, J. Mater. Sci. Tech. 165 (2023) 235–243.
[11] A. Raya-Imbernón, A.A. Samu, S. Barwe, G. Cusati, Ts Fődi, B.M. Hepp, C. Janáky, Renewable syngas generation via Low-Temperature electrolysis: opportunities and challenges, ACS Energy Lett. 9 (2023) 288–297.
[12] Z. Wang, Y. Zhou, P. Qiu, C. Xia, W. Fang, J. Jin, L. Huang, P. Deng, Y. Su, R. Crespo-Otero, X. Tian, B. You, W. Guo, D. Di Tommaso, Y. Pang, S. Ding, B. Y. Xia, Advanced catalyst design and reactor configuration upgrade in electrochemical carbon dioxide conversion, Adv. Mater. 35 (2023) 2303052.
[13] N.T. Nesbitt, T. Burdyny, H. Simonson, D. Salvatore, D. Bohra, R. Kas, W.A. Smith, Liquid-solid boundaries dominate activity of CO_2 reduction on gas-diffusion electrodes, ACS Catal. 10 (2020) 14093–14106.
[14] Z. Wei, W. Wang, T. Shao, S. Yang, C. Liu, D. Si, R. Cao, M. Cao, Constructing Ag/Cu_2O interface for efficient neutral CO_2 electroreduction to C_2H_4, Angew. Chem. Int. Ed. Engl. 64 (2024) e202417066..
[15] M. Yang, J. Wu, Y. Li, H. Pan, H. Cui, X. Lu, X. Tang, Structural evolution of Oxide-Derived nanostructured silver electrocatalysts during CO_2 electroreduction, ACS Catal. 14 (2024) 6169–6178.
[16] W.B. Wan, Y.T. Zhou, S.P. Zeng, H. Shi, R.Q. Yao, Z. Wen, X.Y. Lang, Q. Jiang, Nanoporous intermetallic Cu_3Sn/Cu hybrid electrodes as efficient electrocatalysts for carbon dioxide reduction, Small 17 (2021) 2100683.
[17] X. Yu, Y. Xu, L. Li, M. Zhang, W. Qin, F. Che, M. Zhong, Coverage enhancement accelerates acidic CO_2 electrolysis at ampere-level current with high energy and carbon efficiencies, Nat. Commun. 15 (2024) 1711.
[18] Z. Zhang, G. Wen, D. Luo, B. Ren, Y. Zhu, R. Gao, H. Dou, G. Sun, M. Feng, Z. Bai, A. Yu, Z. Chen, Two ships in a Bottle" design for Zn-Ag-O catalyst enabling selective and Long-Lasting CO_2 electroreduction, J. Am. Chem. Soc. 143 (2021) 6855–6864.
[19] X. Zhang, X. Sun, S.-X. Guo, A.M. Bond, J. Zhang, Formation of lattice-dislocated bismuth nanowires on copper foam for enhanced electrocatalytic CO_2 reduction at low overpotential, Energy Environ. Sci. 12 (2019) 1334–1340.
[20] J. Fan, X. Zhao, X. Mao, J. Xu, N. Han, H. Yang, B. Pan, Y. Li, L. Wang, Y. Li, Large-Area vertically aligned bismuthene nanosheet arrays from galvanic replacement reaction for efficient electrochemical CO_2 conversion, Adv. Mater. 33 (2021) 2100910.
[21] X. Wu, Y. Guo, Z. Sun, F. Xie, D. Guan, J. Dai, F. Yu, Z. Hu, Y.C. Huang, C.W. Pao, J. L. Chen, W. Zhou, Z. Shao, Fast operando spectroscopy tracking in situ generation of rich defects in silver nanocrystals for highly selective electrochemical CO_2 reduction, Nat. Commun. 12 (2021) 660.
[22] Y. Hu, D. Lu, W. Zhou, X. Wang, Y. Li, In situ construction of 3D low-coordinated bismuth nanosheets@cu nanowire core–shell nanoarchitectures for superior CO_2 electroreduction activity, J. Mater. Chem. A 11 (2023) 1937–1943.
[23] E.W. Lees, B.A. Mowbray, F.G. Parlane, C.P. Berlinguette, Gas diffusion electrodes and membranes for CO_2 reduction electrolysers, Nat. Rev. Mater. 7 (2022) 55–64.
[24] F. Pan, Y. Yang, Designing CO_2 reduction electrode materials by morphology and interface engineering, Energy Environ. Sci. 13 (2020) 2275–2309.
[25] H. Rabiee, L. Ge, X. Zhang, S. Hu, M. Li, Z. Yuan, Gas diffusion electrodes (GDEs) for electrochemical reduction of carbon dioxide, carbon monoxide, and dinitrogen to value-added products: a review, Energy Environ. Sci. 14 (2021) 1959–2008.
[26] G. Chen, L. Ge, B. Ma, Y. Kuang, H. Rabiee, F. Dorosti, A.K. Nanjundan, Z. Zhu, H. Wang, Pore accessibility matters in CO_2 electrolysis: preventing H_2 formation

and boosting triple-phase boundary on microtubular gas-diffusion electrodes, Appl. Catal. B 363 (2025) 124803.
[27] G. Chen, L. Ge, Y. Kuang, H. Rabiee, B. Ma, F. Dorosti, A. Kumar Nanjundan, Z. Zhu, H. Wang, Hollow fiber gas-diffusion electrodes with tailored crystal facets for tuning syngas production in electrochemical CO_2 reduction, Chem. Eng. J. 490 (2024) 151651.
[28] Y. Kuang, G. Chen, D.H. Mudiyanselage, H. Rabiee, B. Ma, F. Dorosti, A. K. Nanjundan, Z. Zhu, H. Wang, L. Ge, Engineering interfacial molecular interactions on ag hollow fibre gas diffusion electrodes for high efficiency in CO_2 conversion to CO, Chem. Eur. J. 30 (2024) e202403251.
[29] G. Chen, H. Rabiee, M. Li, B. Ma, Y. Kuang, F. Dorosti, Z. Zhu, H. Wang, L. Ge, Engineering Flow-Through hollow fiber gas-diffusion electrodes for unlocking high-rate Gas-Phase electrochemical conversion, Adv. Mater. 37 (2025) 2420391.
[30] H. Yang, X. Wang, Q. Hu, X. Chai, X. Ren, Q. Zhang, J. Liu, C. He, Recent progress in Self-Supported catalysts for CO_2 electrochemical reduction, Small Methods 4 (2020) 1900826.
[31] B. Zhang, W. Li, J. Jiu, Y. Yang, J. Jing, K. Suganuma, C.F. Li, Large-Scale and galvanic replacement free synthesis of Cu@Ag Core-Shell nanowires for flexible electronics, Inorg. Chem. 58 (2019) 3374–3381.
[32] R. Jiang, V.S. Parameshwaran, J. Boltersdorf, D.R. Baker, Copper-Nanowires incorporated with Silver-Nanoparticles for catalytic CO_2 reduction in alkaline zero gap electrolyzer, ACS Appl. Energy Mater. 6 (2023) 10475–10486.
[33] F. Urbain, P. Tang, N.M. Carretero, T. Andreu, J. Arbiol, J.R. Morante, Tailoring copper foam with silver dendrite catalysts for highly selective carbon dioxide conversion into carbon monoxide, ACS Appl. Mater. Interfaces 10 (2018) 43650–43660.
[34] G. Chen, L. Ge, Y. Kuang, H. Rabiee, B. Ma, F. Dorosti, A.K. Nanjundan, Z. Zhu, H. Wang, In situ growth of hierarchical silver Sub-Nanosheets on zinc Nanosheets-Based hollow fiber Gas-Diffusion electrodes for electrochemical CO_2 reduction to CO, Small Sci. 4 (2024) 2400184.
[35] W. Shan, R. Liu, H. Zhao, Z. He, Y. Lai, S. Li, G. He, J. Liu, In situ Surface-Enhanced Raman spectroscopic evidence on the origin of selectivity in CO_2 electrocatalytic reduction, ACS Nano 14 (2020) 11363–11372.
[36] H.K. Lee, Y.H. Lee, C.S.L. Koh, G.C. Phan-Quang, X. Han, C.L. Lay, H.Y.F. Sim, Y.-C. Kao, Q. An, X.Y. Ling, Designing surface-enhanced Raman scattering (SERS) platforms beyond hotspot engineering: emerging opportunities in analyte manipulations and hybrid materials, Chem. Soc. Rev. 48 (2019) 731–756.
[37] M. Zhao, Y. Gu, W. Gao, P. Cui, H. Tang, X. Wei, H. Zhu, G. Li, S. Yan, X. Zhang, Z. Zou, Atom vacancies induced electron-rich surface of ultrathin bi nanosheet for efficient electrochemical CO_2 reduction, Appl. Catal. B 266 (2020) 118625.
[38] Y. Qin, G. Zhan, C. Tang, D. Yang, X. Wang, J. Yang, C. Mao, Z. Hao, S. Wang, Y. Qin, H. Li, K. Chen, M. Liu, J. Li, Homogeneous vacancies-enhanced orbital hybridization for selective and efficient CO_2-to-CO electrocatalysis, Nano Lett. 23 (2023) 9227–9234.
[39] M. Al-Hada, L. Gregoratti, M. Amati, M. Neeb, Pristine and oxidised Ag-nanoparticles on free-standing graphene as explored by X-ray photoelectron and auger spectroscopy, Surf. Sci. 693 (2020) 121533.
[40] S. Rondinini, O. Lugaresi, E. Achilli, C. Locatelli, A. Minguzzi, A. Vertova, P. Ghigna, C. Comninellis, Fixed energy X-ray absorption voltammetry and extended X-ray absorption fine structure of ag nanoparticle electrodes, J. Electroanal. Chem. 766 (2016) 71–77.
[41] C. Ampelli, F. Tavella, D. Giusi, A.M. Ronsisvalle, S. Perathoner, G. Centi, Electrode and cell design for CO_2 reduction: a viewpoint, Catal. Today 421 (2023) 114217.
[42] H. Rabiee, L. Ge, X. Zhang, S. Hu, M. Li, S. Smart, Z. Zhu, H. Wang, Z. Yuan, Stand-alone asymmetric hollow fiber gas-diffusion electrodes with distinguished bronze phases for high-efficiency CO_2 electrochemical reduction, Appl. Catal. B 298 (2021) 120538.
[43] Z. Geng, X. Kong, W. Chen, H. Su, Y. Liu, F. Cai, G. Wang, J. Zeng, Oxygen vacancies in ZnO nanosheets enhance CO_2 electrochemical reduction to CO, Angew. Chem. Int. Ed. Engl. 57 (2018) 6054–6059.
[44] H. Rabiee, L. Ge, J. Zhao, X. Zhang, M. Li, S. Hu, S. Smart, T.E. Rufford, Z. Zhu, H. Wang, Z. Yuan, Regulating the reaction zone of electrochemical CO_2 reduction on gas-diffusion electrodes by distinctive hydrophilic-hydrophobic catalyst layers, Appl. Catal. B 310 (2022) 121362.
[45] S. Li, W. Chen, X. Dong, C. Zhu, A. Chen, Y. Song, G. Li, W. Wei, Y. Sun, Hierarchical micro/nanostructured silver hollow fiber boosts electroreduction of carbon dioxide, Nat. Commun. 13 (2022) 3080.
[46] A. Chen, X. Dong, J. Mao, W. Chen, C. Zhu, S. Li, G. Wu, Y. Wei, X. Liu, G. Li, Y. Song, Z. Jiang, W. Wei, Y. Sun, Gas penetrating hollow fiber bi with contractive bond enables industry-level CO_2 electroreduction, Appl. Catal. B 333 (2023) 122768.
[47] A. Chen, C. Zhu, J. Mao, S. Li, G. Wu, Y. Wei, X. Liu, X. Dong, Y. Song, G. Li, Y. Sun, W. Wei, W. Chen, Hollow penetration electrode of bi with dislocated lattice enabling ampere-level reduction of CO_2 exclusively to formate, Appl. Catal. B 343 (2024) 123493.